WPMST1-PR(17) 18514

S Zoletnik et al.

Ultrafast Twodimensional Lithium Beam Emission Spectroscopy Diagnostic on the EAST Tokamak

Preprint of Paper to be submitted for publication in
Review of Scientific Instruments

This work has been carried out within the framework of the EUROfusion Consortium and has received funding from the Euratom research and training programme 2014-2018 under grant agreement No 633053. The views and opinions expressed herein do not necessarily reflect those of the European Commission.

Ultrafast Twodimensional Lithium Beam Emission Spectroscopy Diagnostic on the EAST Tokamak

S. Zoletnik,[1] G.H. Hu,[2] B. Tál,[1] D. Dunai,[1] G. Anda,[1] O. Asztalos,[3] G. I. Pokol,[3] J. Németh,[1] and T. Krizsanóczi[1]

[1)] *Wigner Research Center for Physics, Budapest, Hungary*

[2)] *Institute for Plasma Physics, Chinese Academi of Scienes, Hefei, China*

[3)] *Budapest University of Technology and Economnics, Budapest, Hungary*

(Dated: 15 November 2017)

A diagnostic instrument is described for the EAST tokamak for the measurement of edge plasma electron density profile and plasma turbulence properties. An accelerated neutral Lithium beam is injected into the tokamak and the Doppler shifted 670.8 nm light emission of the Li2p-2s transition is detected. A novel compact setup is used, where the beam injection and observation takes place from the same equatorial diagnostic port and radial-poloidal resolution is achieved with microsecond time resolution. The observation direction is optimized in order to achieve sufficient Doppler shift of the beam light to be able to separate from the strong edge Lithium line emission on this Lithium coated device. A 250 kHz beam chopping technique is also demonstrated for the removal of background light. First results show the capability of measuring turbulence and its poloidal flow velocity in the scrape-off layer and edge region and resolution of details of transient phenomena like ELMs with few microsecond time resolution.

PACS numbers: 52.70Kz, 52.55Fa, 52.35Ra

I. INTRODUCTION

The boundary of magnetically confined fusion plasmas is of special importance for the quality of plasma confinement. It consists of two different layers around the Last Closed Flux Surface (LCFS) or separatrix. The edge plasma which is just inside the LCFS where the plasma is still confined and the Scrape Off Layer (SOL) which is outside the LCFS where magnetic field lines end on material surfaces. SOL parameters define the gas recycling, impurity production from, and heat load to limeters or divertor plates. Cross-field transport in both of these areas is known to be dominated by plasma turbulence. In the edge plasma turbulence is suppressed when the H-mode transition occurs and a pedestal develops with steep temperature and density gradients. Although the H-mode transition is not fully understood there is agreement that strongly sheared poloidal flows play a crucial role in it. The low transport across the pedestal is regularly bypassed by the Edge Localized Mode (ELM) instability which ejects plasma into the SOL. This process is both beneficial for improved density and impurity control and at the same time dangerous due to the heat load the the divertor. Understanding and controlling ELMs is a key issue for future fusion experiments. In the SOL transport is carried by a special type of turbulence, radially outward propagating blobs (field-aligned plasma filaments) originating around the LCFS[1]. Their dynamics determine the SOL width as recently emphasized by the formation of a so-called density-shoulder[2].

Due to the above reasons measuring the profiles, turbulence and flows in the full SOL-edge region is a key fusion diagnostic task. Due to the statistical nature of turbulence and the fast phenomena related to ELMs and blobs time resolution on the microsecond timescale is necessary preferably with cm or better spatial resolution on a two-dimensional (radial-poloidal) area. This requirement is fulfilled only by a few diagnostics[3]. In the SOL various probes can provide measurements of the plasma density, potential and temperature with good localization but only at few points. On larger high power devices the probe measurements cannot access the edge region, especially in H-mode, therefore probes are generally usable in the SOL only. Gas-puff imaging (GPI) can access a small region at both sides in the LCFS therefore could provide essential 2D information on turbulence and flows through the movement of turbulence structures. Indeed detailed information was obtained both in L and H-mode[4,5] and on the interaction between flows and turbulence[6,7]. Despite

of these excellent possibilities the basic limitation of GPI is that it provides information on an unknown combination of various plasma parameters and, due to its limited spatial range, cannot measure parameter profiles. Various reflectometry schemes[8] are capable of measuring density fluctuations, flows and profiles with excellent sensitivity and temporal resolution and indeed revealed details of flow-turbulence interactions[9,10] in the edge region. However, for strongly non-monotonic density profiles (e.g. during ELMs and SOL blobs) reflectometry has interpretation difficulties. Various versions of Beam Emission Spectroscopy (BES) diagnostic[11] are also used extensively in the edge plasma. They measure the light emitted by a neutral atomic beam as it penetrates the plasma. The beam atoms are excited by collisions with plasma electrons and ions and the intensity of the line radiation reveals information on the exciting plasma, mostly on its electron density. In case of a Hydrogen isotope heating beam (H-BES) special geometry has to be used for the observation. It has to provide sufficient Doppler shift of the beam line radiation to distinguish it from the much stronger edge plasma emission and at the same time to view along magnetic field lines so as to have sufficient spatial resolution across the field. Such schemes have been implemented on various devices and yielded detailed information on plasma turbulence and zonal flows in the core-edge region[12–14].

Another version of BES uses a narrow Lithium beam (Li-BES) this way relaxes the limitations on the observation geometry. Li atoms have higher ionization rates in the plasma therefore the beam penetrates only the edge plasma before ionizing. This means it is inherently an edge diagnostic, but also has an important advantage. Following the beam light emission until the beam is to some extent ionized enables one to calculate the absolute electron density profile from the relatively calibrated light profile[15,16]. Indeed Li-BES was developed for edge density profile measurement[17–19]. With high-frequency light detectors measurement of density fluctuations resulting from plasma turbulence became possible[20–23]. Although the narrow beam would allow only one-dimensional (radial) resolution a quasi-2D scheme has been demonstrated by a hopping beam[24,25] which extends the possibilities to poloidal flow velocity measurement. With these developments the Li-BES diagnostic technique became capable of measuring the density profile, turbulence and flows from the SOL to the edge region.

Although in theory these Li-BES schemes would provide an ideal diagnostic for measuring profiles, flows and turbulence in the SOL-edge plasma the actual implementations have seri-

ous difficulties. The most important limitation is the detected photon flux. On Wendelstein 7-AS[22], ASDEX Upgrade[19,23] and JET[26] SOL turbulence measurements became possible but the signal-to-noise ratio (SNR) of the signals did not allow regular edge turbulence measurements. On TEXTOR a high-Etendue optics and improved detectors were installed which did enable edge turbulence and zonal flow measurements[25] and observation of details of ELMs[27]. However, the poloidal view on the beam still limited the diagnostic to quasi-2D resolution at a limited 250 kHz temporal resolution. This was first overcome on KSTAR with the injection of a Li-Beam into the observation volume of a H-BES diagnostic[28]. This field-parallel 2D view provided radial-poloidal resolution but the light intensity was still to some extent limited by the relatively small Etendue of the optics. The aim of this paper is to describe a diagnostic setup on the Experimental Advanced Superconducting Tokamak (EAST) which combines high collected light intensity, two-dimensional resolution and large enough radial measurement range to allow measurement of profiles, turbulence and poloidal flows.

The paper is organized as follows. Section II describes the considerations for the layout of the system, especially the location of the observation port. The Li-beam injector setup is described in a separate paper[29], the observation system hardware is detailed in Section III. Due to their importance Sections IV and V are devoted to calibration and background correction techniques. Some illustrative results are presented in Section VI and the paper closes with the Conclusions.

II. DESIGN CONSIDERATIONS

The EAST tokamak is a middle-size superconductive fusion experiment with major radius 1.85m and minor radius 0.45 m. Diagnostic and heating access is mostly possible through 16 large rectangular horizontal ports on the outer equatorial plane of the device. Being a superconducting machine the plasma vacuum vessel is surrounded by a cryostat with about 1.5 m distance from the plasma to the cryostat port end. Due to space limitations the Li-beam injector had to be located about 4 m from the observation volume in the plasma. At this distance the beam FWHM was expected to be 2-3 cm. To be able to measure poloidal flows the optical resolution has to be somewhat better than the beam width. Therefore, the design aim of the optics was to set up a Li-BES diagnostic with about 1 cm radial-

poloidal resolution and maximum light collection solid angle. The ideal solution would be to inject the beam horizontally and observe from a neighboring port with a large diameter first lens, as done in the KSTAR BES system[28]. Due to the crowded horizontal ports this was not possible, therefore observation on the same port as the injection was considered. The Li-beam is injected at the equatorial plane on the right hand side of port D while the observation window was sought to be placed onto the left side of the 450 mm wide port at the end of an air filled tube. The center of the radial observation range in the plasma was set to R=224 cm, while the plasma separatrix is normally located at about R=230 cm.

In order to keep enough clearance to the plasma edge the observation window center was placed at R=276 cm which is inside the cryostat port. Placing the window also at the equatorial plane would have meant 35 degree observation angle relative to the beam at the center of the observation range. For the expected 3 cm upper bound on the beam diameter the radial smearing due to the intersection of an observation line with the beam would have been about 5 cm. This was expected to be too much for reconstructing the radial density profile, therefore the observation system was moved to 35.8 cm above the equatorial plane. At this position the radial smearing is reduced to about 3 cm while about 2 cm poloidal smearing is introduced due to the large angle between the line of sight and the magnetic field. This radial smearing is about the same as the one introduced by the lifetime of the excited Li atom state. Density reconstructions from modeled light profiles confirmed that at this radial smearing measuring the light profile with 1 cm resolution for at least 20 cm radial range the expected density profiles can be reconstructed.

The calculated Doppler shift of the 50 keV Li-beam for this geometry is 1.5-2.2 nm. This is sufficiently large to enable separation from the unshifted Li resonance line at 670.8 nm, expected to be strong due to large amount of Lithium used for wall conditioning on EAST. Figure 1 shows the final geometry of the diagnostic. A disadvantage of this setup is that the optics looks into the divertor, which is expected to be a strong radiation source.

The beam light emission was modeled in detail using the RENATE 3D beam modeling code[30] and density profile reconstructions were done for different modeled density profiles based on measured density data from shot 33068 at 2750 ms, with the corresponding magnetic geometry. 2 cm FWHM diameter Lithium beam was assumed with a beam energy of 50 keV, beam current of 1 mA. The observation system was modelled as a 4 x 32 APD pixel grid, realizing 1 cm sized detector pixel projections on the focal plane of the observation

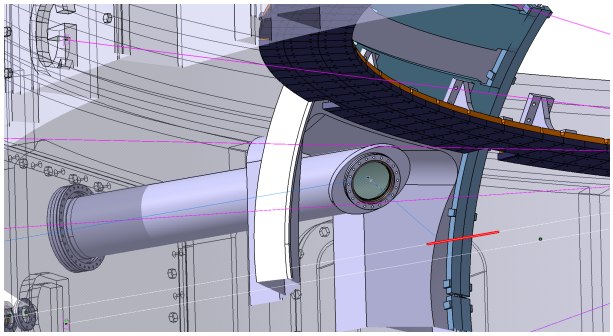

FIG. 1. Geometry of the EAST Li-BES diagnostic. The red line indicates the observation range along the Li-beam.

system as shown in Figure 4. Figure 2 (a) shows the density profile along the beam as well as the calculated emission profile peaking at 2.26 m, 4 cm inside the separatrix. The photon flux collected by each detector is calculated by modeling the light collection in the actual observation geometry and assuming 50% overall detection efficiency (optics, filter throughput and detector efficiency). The resulting photon count is shown in Figure 2(b). Modelling projects a detected peak photon flux in the range of $10^{10} ph/s$, which provides a strong signal with 1-2% statistical noise at an analogue bandwidth of 500 kHz. In the SOL region the photon flux is in the $10^{9} ph/s$ range with 3-5% expected noise level on 500 kHz bandwidth. This is still reasonable for SOL turbulence observation as the expected density fluctuation level is well over 10%. Beam penetration at various plasma density scenarios was determined as shown in Figure 2(c) by scaling the density profile with a factor of 2 (high density scenario) and 4 (ultra-high density scenario). The increase in density improves significantly the amount of detected light in the SOL region, but the emission peak on the detectors is well inside the separatrix for all density scenarios presenting a beam penetration depth of 7 to 3 cm depending on the plasma density.

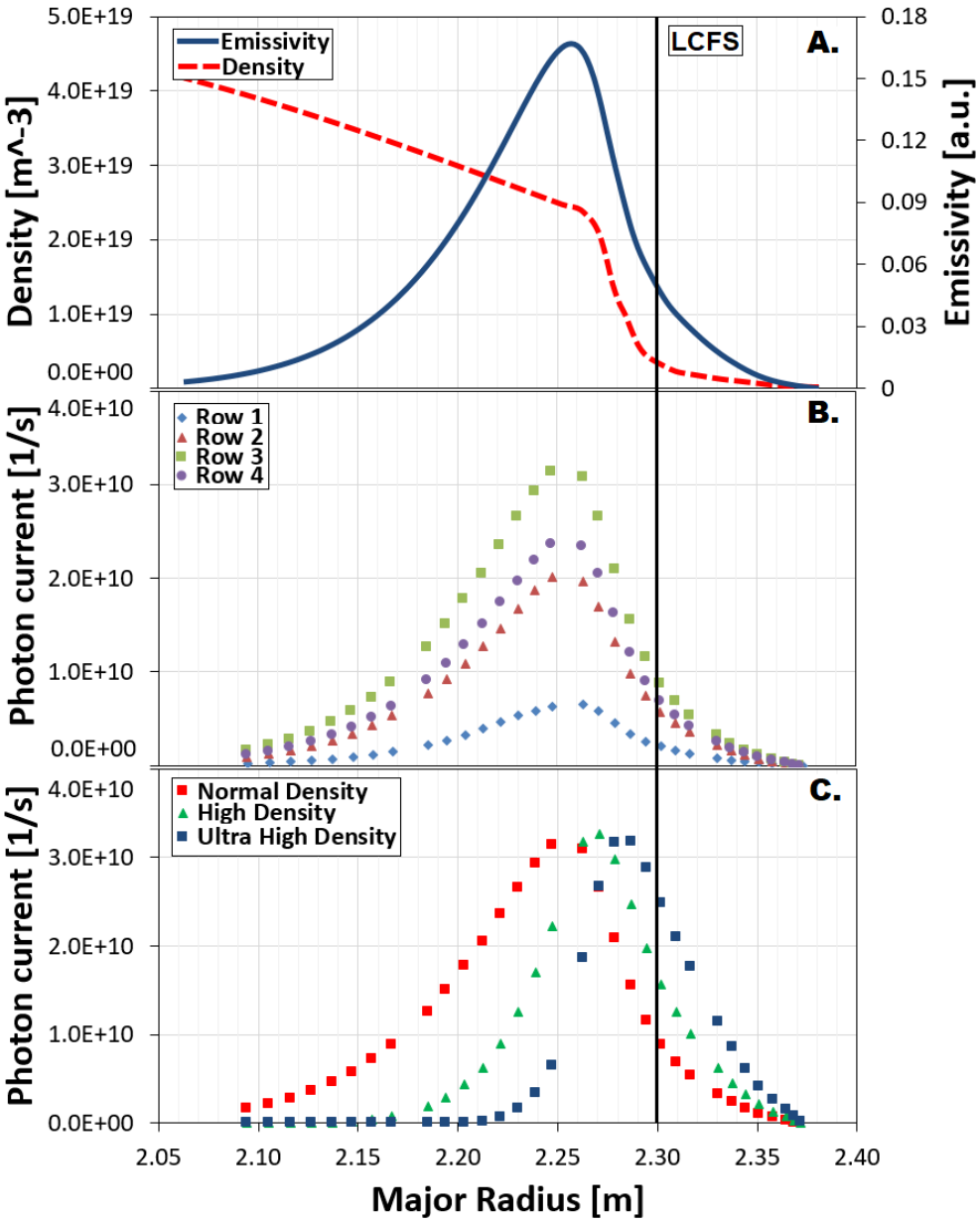

FIG. 2. Modelling of the EAST LiBES system. (a) Density and emission profile along the beam. (b) Detected photon current on all detector rows. (c) Detected photon current on row 3 for various plasma densities.

III. HARDWARE SETUP

A. Optics

The optics concept defined two detectors for the system: a CMOS camera for overview of the beam image in the plasma and an Avalanche PhotoDiode (APD) detector matrix camera

for performing fast measurements. The CMOS camera is intended for slow measurements and to monitor the beam shape. It receives only less than 10% of the light, most of the light is directed to the APD camera. The optical design is shown in Figure 3. The front part of the optics is located in a vacuum tube with a window on the the front. The first optical element is an 80 mm diameter lens located at about 65 cm from the center of the observation area. The optical axis is turned horizontal by a prism and a series of lenses transmit the light out from the vacuum tube where an approximate intermediate image is formed. A pneumatically operated screen can be placed here for spatial cross calibration of the two detectors as described below. The optical axis is turned vertical by a mirror. A small mirror directs a few percent of the light in a Fourier plane towards the CMOS camera. Due to the small mirror the CMOS camera has higher field of depth which can be even increased by limiting the light with a pneumatically operated small diaphragm. Most of the light is passing the small mirror and finally imaged into an APD camera. As the Li-beam is not perpendicular to the optical axis the image plane is also tilted. Therefore the detector plane of the camera is tilted relative to the optical axis such that the detector is in the image plane. The whole camera can be moved along the detector axis with a precise stepmotor drive. Separate interference filters are used for the CMOS and APD branch, both can be moved in-out with a pneumatic actuator.

B. Filter design

On EAST Lithium is evaporated onto the vacuum vessel wall for wall conditioning and occasionally also Lithium is injected during the discharge for plasma control. Under these conditions neutral Lithium atoms are abundant in the edge plasma and the 670.8 nm line radiation is strong. The red Doppler shift for the Li-beam atoms is 1.5-2.5 nm depending on beam energy and location along the beam. Although some Carbon lines are also present in the 671-673 nm wavelength range[31] the filter design criterium was to suppress the 670.8 nm line by at least a factor of 1000 while keeping the transmission above 672.3 nm as high as possible. As the interference filters are angle sensitive the optical design criterium was to keep the light ray angles on the filter below 3 degrees where the wavelength shift is small. The resulting filter in the APD branch is large, 165 mm in diameter. To select the filter parameters a modeling code was developed. The first lens surface was divided into small

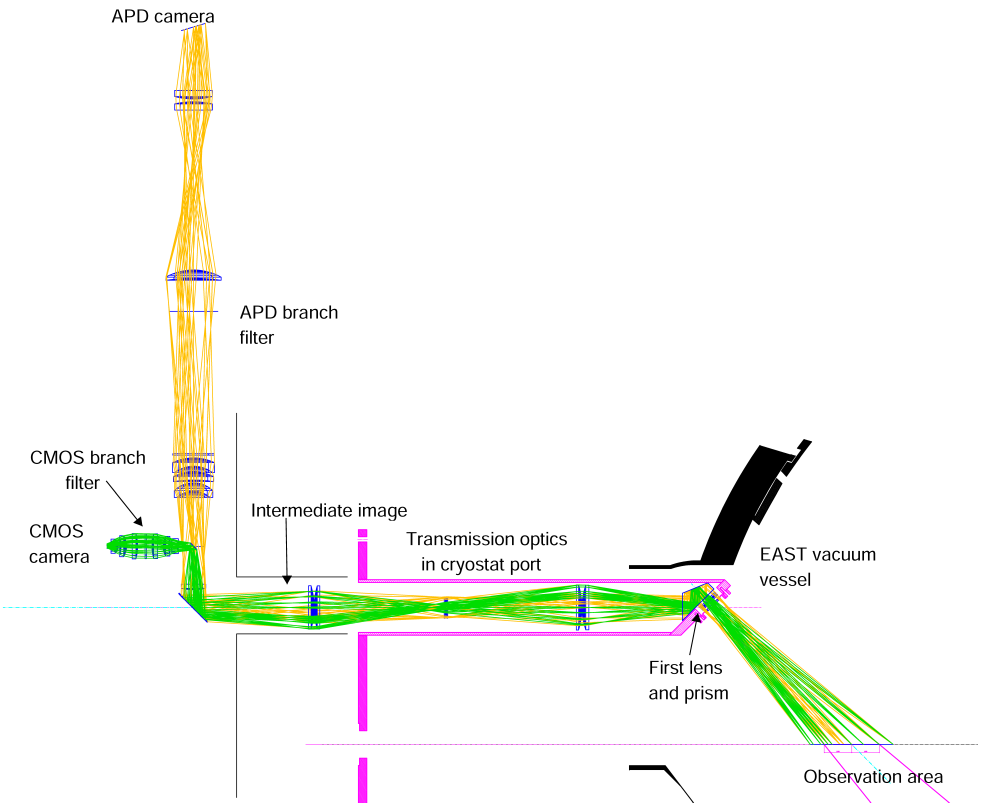

FIG. 3. Optical design of the EAST Li-BES diagnostic. The plane of the design is inclined, going through the beam and the center of the first lens. The part after the turning mirror is rotated vertical in real geometry by selecting a suitable mirror inclination.

areas and light rays were considered from the beam to their center. The angular distribution of these light rays on the filter was determined from the Zemax optical design software. The theoretical transmission curves of filters as a function of wavelength, angle and temperature were obtained from potential manufacturers. The theoretical transmission of the Doppler shifted beam light and of the unshifted 670.8 nm light was calculated and summed up for all light rays. Zeeman split was not considered for the beam light as the broadening is in the 0.05 nm range[?] , much less than the change of the Doppler shift along the beam. The filter central wavelength (CWL) and bandwidth (BW) were varied until the beam light transmission was close to maximum while the transmission of the unshifted Lithium light remained below 0.1%. The effect of CWL manufacturing tolerance and nonuniformity across the filter surface was also modeled and they were found to be critical. Finally an offer was obtained from Andover Co. for an 1±0.2 nm BW filter with +0.2, -0 nm CWL tolerance

which was considered to be suitable. Even with this low tolerance the filter performance would have been significantly dependent on the final manufacturing outcome. To compensate for this the temperature sensitivity of this filter (0.018 nm/C shift in CWL) was considered. The CWL was modified so as that even in the uppermost position of the short wavelength cutoff enabled by the tolerance the filter performs optimally. 0.4 nm downshift of this cutoff is enabled by the tolerance which can be compensated by 22 Celsius increase of the filter operating temperature, therefore the manufacturing tolerance of the filter can be fully compensated if the filter temperature can be kept uniform to better than 10 degrees C. The resulting filter parameters are BW=1.0 nm, CWL=672.2 nm which was used for both filters in the diagnostic.

In order to control the filter temperature a filter holder was designed where the filter sits in a thermally isolating plastic ring and covered on both sides with double 1 mm thick antireflection coated windows. The air gap between the two glass plates serves for thermal isolation. In the gap between the filter and the inner glass plate hot air is circulated by miniature air blowers. The air is heated (but not cooled) by a resistor chain and the filter temperature is measured on its edge in order to control the heating power with a PID temperature controller. The operation of the setup was modeled with a dummy filter and it was found that the filter temperature distribution can be kept uniform within 5-7 C up to the maximum 60 C allowed by the filter manufacturer. This setup also enables to modify the filter performance and further increase the suppression of the unshifted Li line at the expense of some loss in beam light transmission at the plasma edge. An alternative filter with 0.8 nm BW and somewhat upshifted steeper short-wavelength cutoff is also being tested from Materion Co. This indeed increased background suppression at the expense of stronger cut of beam light in the scrape-off layer (SOL) and edge region.

Although considerable effort was devoted to the filter optimization it was expected that the background light would not be negligible. To measure it a fast beam modulation (chopper) is installed in the beam injector which can switch on-off the beam with up to 250 kHz frequency[24]. Beam chopping is synchronized to the light measurement therefore high frequency beam and background signals can be calculated.

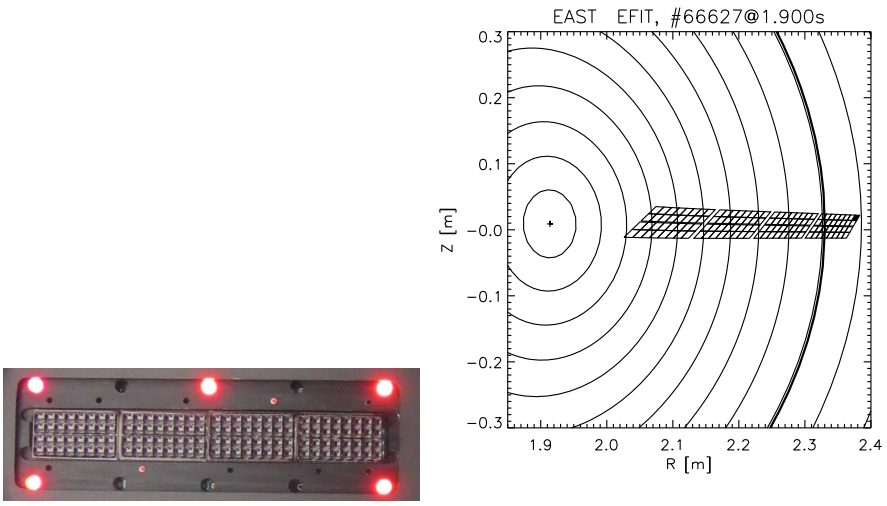

FIG. 4. Photograph of the APD detector matrix with calibration LEDs and optical fibres (small red dots) and the outline of APD pixel coordinates mapped to the vertical beam plane overlaid to the EFIT plasma equilibrium reconstruction. The thick line indicates the separatrix, the filled pixel is row 1 column 1.

C. Detectors and control system

The main detector of the diagnostic is a 4x32 pixel APD detector matrix (APDCAM-10G-4x32 from Fusion Instruments, see Figure 4) with micro-lens array. The micro-lens array increases the 50% fill factor of the Hamamatsu S8550 APD matrix to nearly 100% by focusing light from the microlens surface to the sensitive detector areas. The analog amplifiers are set to 500 kHz bandwidth, about 2.7 mV noise and $3.2 \cdot 10^{-11}[Vs]$ sensitivity. ($3.2 \cdot 10^{-11}V$ signal for $1s^{-1}$ detected photon flux with standard 50 detector gain.) The 2.3x2.3 mm pixels of the detector are imaged to about 1 cm on a vertical plane along the Li-beam, thus about 32 cm is covered radially and 4 cm poloidally. The detector signals can be sampled with maximum 4 MHz/14 bit rate for at least 10 s although in most cases only 1 or 2 MHz is used. The APDCAM camera head contains two optical fibres for spectral measurements around the detector and LEDs for spatial calibration. A PhotonFocus MV1-D1312(IE/C)-G2 CMOS camera receives a few percent of the light and can take images of the beam 2D shape.

Data are acquired with a Personal Computer. The APDCAM camera uses 10 Gbit, while the CMOS camera 1 Gbit optical Ethernet communication and collects data directly to

the 16 Gbyte PC memory during the discharge. The sampling of both detectors is based on a common clock signal from the EAST data acquisition system so as timing is fixed to other diagnostic. Various actuations and the filter temperature in the optical setup are controlled from the same PC using Ethernet-based digital switches and a temperature controller instrument. The whole system can be remotely controlled from the EAST control room.

IV. CALIBRATION

A. Spatial calibration and sensitivity

The optics was assembled in a laboratory and the imaging was tested by observing an object screen and the image of LEDs in a vertical plane along the expected beam center. The location of the screen was measured relative to the frontend optics, therefore the spatial calibration of the system relies on exactly knowing the location of the EAST port flanges, which was measured in the machine by a robotic arm.

The calibration procedure works as follows. Pictures of the screen in the object plane are taken with the CMOS camera and an array of known points with $\mathbf{P}_i = (R_i, Z_i, \phi_i)$ object space coordinates are marked on the images: x_i, y_i. Here R, Z and ϕ are major radius, elevation from the equatorial plane and toroidal angle, respectively. A point and two unit vectors are assumed to be known which describe the imaging: the principal point ($\mathbf{O}$), the direction of the optical axis in the tokamak ($\mathbf{n}_1$) and the direction of the image of the x axis of the CMOS camera detector in the object plane ($\mathbf{n}_2$). From these the projection of the points to the plane perpendicular to the observation direction is calculated:

$$\bar{\mathbf{P}}_i = \mathbf{P}_i - [(\mathbf{P}_i - \mathbf{O}) \cdot \mathbf{n}_1]\, \mathbf{n}_1. \tag{1}$$

The projection of $\bar{\mathbf{P}}_i$ to $\mathbf{n}_2$ is assumed to be related to the x coordinate of the point's image on the CMOS camera, while the projection perpendicular to $\mathbf{n}_2$ is related to the y coordinate:

$$a_i^x = \bar{\mathbf{P}}_i \cdot \mathbf{n}_2 \tag{2}$$

$$a_i^y = \bar{\mathbf{P}}_i \cdot (\mathbf{n}_1 \times \mathbf{n}_2) \tag{3}$$

To allow for any magnification, shift and distortion K^x and K^y matrices of a bilinear trans-

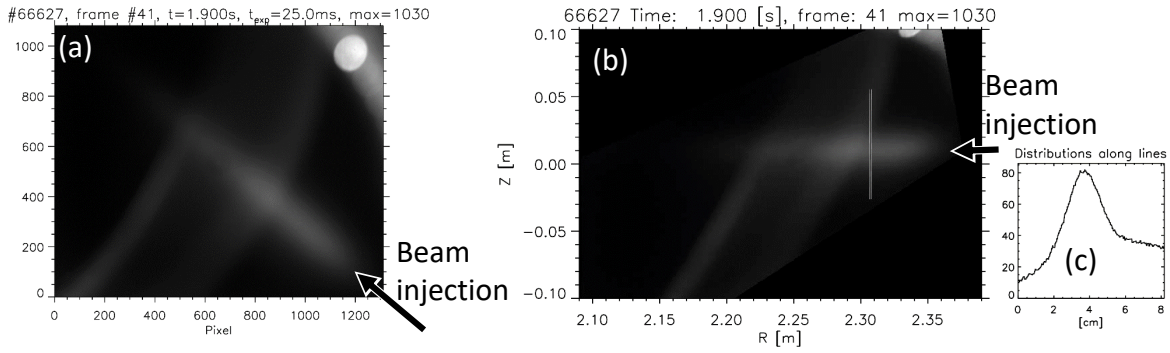

FIG. 5. A CMOS camera image (a) and image mapped to beam plane (b). On plot (c) the intensity distribution is plotted along the vertical line in plot (b). The asymmetric profile is due to the asymmetric background.

formation from the a_i^x and a_i^y coordinates to x_i, y_i are fitted:

$$x_i = \sum_{k,l=0}^{1} K_{kl}^x \left(a_i^x\right)^k \left(a_i^y\right)^l \tag{4}$$

$$y_i = \sum_{k,l=0}^{1} K_{kl}^y \left(a_i^x\right)^k \left(a_i^y\right)^l \tag{5}$$

Due to this fitting step the $\mathbf{O}$, $\mathbf{n}_1$ and $\mathbf{n}_2$ parameters serve only for initializing the fitting procedure, their values need not be exact. Knowing the K^x and K^y matrices any point can be mapped from the 3D tokamak coordinates to the 2D CMOS image. A rectangular mesh of points are taken in the vertical beam plane and mapped to the CMOS image. A second set of mapping matrices are fitted to the mapping of these points from the 2D CMOS image to the 2D beam plane. With this all CMOS image points can be mapped to the beam plane and the image of the CMOS camera can be mapped to the R, Z tokamak plane. An example is shown in Figure 5. Considerable background is present from the limiter region. The beam width is about 2.5-3 cm.

The spatial calibration of the APD camera is based on the CMOS image calibration. A screen is introduced into the intermediate image plane (see Figure 3), the calibration lights on the APD camera (see Figure 4) are switched on and their image is observed with the CMOS camera. The LED image positions are marked and a bilinear transformation is fitted between the APD detector plane and the CMOS image coordinates. As the position of the

detector pixels relative to the calibration LEDs is known the detector pixels can be mapped to the CMOS image and from there the beam plane R,Z coordinates as shown in Figure 4. The gaps in the pixel matrix are due to the pixel layout of the Hamamatsu S8550 APD matrix used in this camera. Due to the oblique view the APD pixel images are slanted and the size increases as we look deeper into the plasma. The radial measurement range of the APD system is larger than needed for a standard plasma configuration but we kept this larger range to enable measurement in shifted configurations as well.

The spatial sensitivity of the APD matrix shown in Figure 4 would correspond to the effective sensitivity of the measurement in the tokamak coordinates only if the Li-beam was an infinitely thin vertical plane. In reality one APD pixel collects beam light from a volume defined by the intersection of the optical view and the Li-beam. This is taken into account the following way. The sensitivity volume of one APD pixel is approximated by a prism. Each of the four bounding planes are defined by an edge of a pixel image in the beam plane and the observation direction. (Vector from the center of the pixel image to the center of the first lens.) The beam is modeled having Gaussian intensity distribution with 2.5 cm FWHM with a centerline 1 cm above the midplane as determined from the CMOS camera image. Along the beam uniform intensity is assumed and this radiation source is intersected by the observation volume. The resulting 3D radiating volume is finally integrated perpendicularly to the vertical beam plane to yield an effective sensitivity area of an APD pixel in the R,Z plane. This procedure assumes uniform plasma parameters in the toroidal direction and does not take into account the field line curvature or inclination due to the poloidal field. Due to the small beam FWHM these effects will cause only a few mm error in the calculation which is much smaller than the approx. 10 mm pixel image size.

An example result of this calculation is shown in Figure 6. The colored dots mark the center of the sensitivity areas for all pixels, they are clearly more close to each other then the pixel image centers. The 50% sensitivity curves extend to about 2 cm radially and poloidally and a considerable overlap is present between neighboring pixels in the poloidal direction. The sensitivity curves have an inclined shape due to the oblique observation. This has to be taken into consideration in turbulence velocity calculation with time delay estimation as apparent radial/poloidal velocities might appear in the correlation calculation.

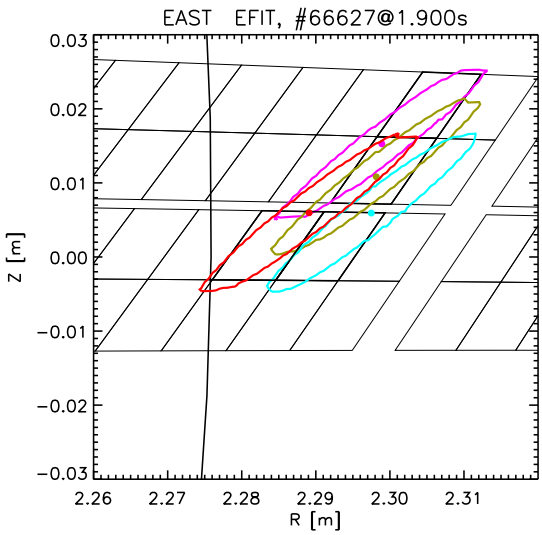

FIG. 6. Calculated R,Z sensitivity distribution of 4 selected APD pixels. The image of the four pixels on the beam plane is marked by thick line. The dots indicate the center of all the APD pixels sensitivities, the elliptic curves mark the 50% sensitivity contours of the 4 selected pixels.

B. Relative amplitude calibration

The optics, filters, detectors all represent spatially variable light detection efficiency, therefore a relative calibration of the system is necessary. This is accomplished using the traditional method[16] of injecting the beam into gas and observing the light emission. If the gas density is sufficiently low the beam is not attenuated and the light emission is uniform along the beam trajectory. The light profile measured in the detectors represent the relative sensitivities and thus used as a calibration factor. In several other experiments calibration is difficult as the signal in the gas is low. As the EAST Li-BES detection system has a high Etendue optics, the signal is well observable even at low gas pressure in both the CMOS and APD detectors. Even no special gas pulses are required, the residual gas in the chamber after the discharge is sufficient to calibrate the system. The beam is modulated (chopped) by deflection plates in order to measure the electronic offset and any background light. The signal in the beam-on and beam-off times is summed in a 1-2 second long time interval and subtracted to yield the relative sensitivity of the measurement channels.

The calibration factors for the APD detector in shot 66627 are shown in Figure 7. The four curves represent the 4 rows of APD detectors, the different intensities are due to the finite beam width. Normalizing the signals in the plasma with these calibration factors

gives the calibrated signals in case of a uniform beam profile. However, slight changes in the beam width or position considerably change the calibration factors, therefore the amplitude calibration across the beam is not reliable. The relative calibration along the beam is less sensitive as the APD pixel rows are arranged along the beam. Nevertheless small systematic changes in the light intensity along the beam might occur in response to beam position and profile changes, therefore it is more reliable to sum up the light intensity in all 4 rows and calculate plasma density from this data. The drop in the calibration factors outside the separatrix (2.3 m) is due partly to vignetting of the optics and partly to cut by the filter. The optics was designed for full transmission for 20 cm and some loss was allowed outside it. However, the strong drop in the SOL is not ideal therefore about 5-10 cm outward shift of the observation range is planned in the future.

Calibration of the CMOS camera observation is done by first mapping the camera image to R-Z plane as shown in Figure 5. Beam on and beam off images are averaged and the two averages subtracted to yield a mean beam light image. The beamline centerline is determined by finding maxima along lines perpendicular to the expected beamline and fitting a straight line to the maximum locations. The light intensity is calculated in narrow stripes perpendiculary to the beamline and thus the calibration factors for these stripes are calculated. These calibration factors are used in calculation of the light profile along the beam in plasma experiments when the light profile is calculated using similar stripes.

The relatively calibrated light distributions along the beam are used for calculating the absolute plasma density profile with an implementation of the Bayesian algorithm described in Ref.[16].

V. BACKGROUND CORRECTION

Part of a Li-beam signal is shown in Figure 8 around the maximum of the light profile. The sharp up-down jumps in the signal are due to Li-beam on-off via the chopper which was synchronized to the CMOS camera measurement in this discharge. The chopper consists of a pair of deflection plates located before the neutralizer and fast voltage switches. When 1 kV is switched on the deflection plates the beam is moved out of the observation volume.

Despite of the high time resolution (500 kHz bandwidth) the signal noise is low, but a few 10% background signal is present. In the stable L-mode part of the discharge (before

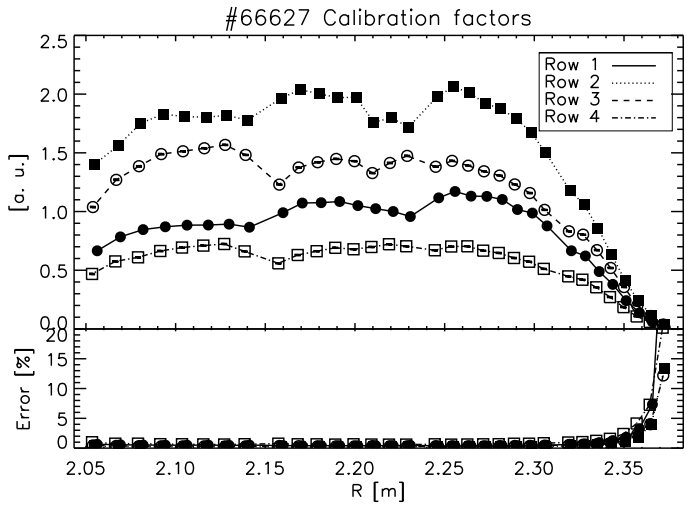

FIG. 7. Calibration factors of the APD camera and estimated relative error in shot 66627. The radial coordinate is the pixel image center.

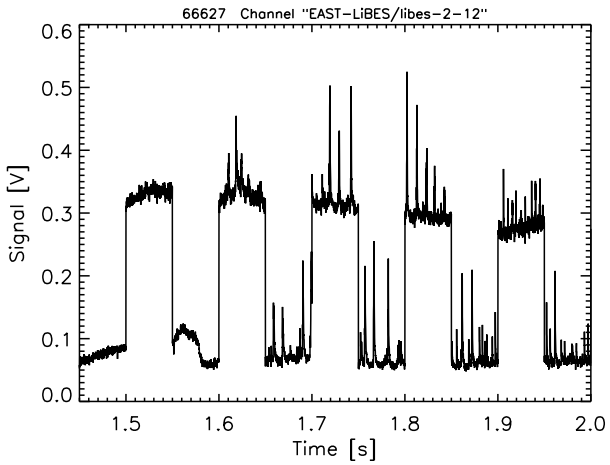

FIG. 8. Example signal of the Li-BES diagnostic in L and H mode. The L-H transition occurs at 1.58s.

1.55s) this is less of a concern as the background is changing slowly. In H-mode the sharp peaks are Edge Localized Modes (ELMs) which strongly modulate the signal. Comparing the ELMs when the beam is on and when it is off one can see that most of the signal change during ELMs comes from the background, therefore the slow chopping mode is not suitable for measuring the fast changes during ELMs, although the SNR and signal bandwidth would be perfect for this.

In order to enable fast measurements even during strong background change the chopper

can be operated at high frequency, up to 250 kHz. This is sufficiently fast to follow the background change during ELMs but also close to the bandwidth of the signal amplifiers. As described in Ref.[24] the beam switches on and off in about 100 ns but with its approximately $10^6 m/s$ velocity it covers the 4 m distance from the chopper to the observation volume in about 4 microseconds and travels through the observation volume in about 300 ns. These times are comparable to the typical 500 ns sampling time resolution of the ADCs, therefore have to be taken into account.

A numerical method has been developed to process the measurements with fast chopping and calculate a background and a beam signal from each measured light signal. The process is illustrated in Figure 9. The beam chopping is synchronized to the signal sampling such that the sampling frequency is an integer number times the chopping frequency. The ADC sampling time jitter is only a few ns, therefore the beam signal evolution in the chopper periods is very reproducible. Signal processing starts with determining the average signal time evolution during a chopper cycle. This is done by averaging each measured signal over many deflection periods, preferably when the plasma is stable. As the fluctuations in plasma density and background are not correlated to beam chopping the resulting average signal is considered as the modulation time evolution of the beam signal taking into account the beam switching time, flight time and finite amplifier bandwidth. This signal we call reference signal $S_{ref}(t), t = [0, T]$, where T is the chopping period time. The reference signal is slightly different for each channel as the beam flight time causes a channel-to-channel time delay. In reality $S_{ref}(t)$ is measured at $N_{ref} = T/\tau_{samp}$ times, where τ_{samp} is the sampling time resolution of the signal. N_{ref} is typically 6-10. The reference signal is scaled in amplitude between 0 and 1 and assumed that when it is 0 (at its minimum) the beam is completely switched off, that is the signal consists of a background and a fully modulated beam signal. If the beam is not switched completely off than some part of the beam signal will be treated as background. The beam-on time is determined from the reference signal where the signal is above 0.2. The reference signal is cyclically shifted until first signal is beam-off and the second signal is beam-on. Also the start of the measurement signal is shifted until the first sample is beam-off and the second beam-on. If there are multiple beam-on switching times in the reference signal it is considered as unusable and a reference signal is generated by temporally shifting and averaging other reference signals in the same pixel row along the beam. After calculating these reference signals for each of the 128 APD channels from a

suitable time interval they are used for any other time interval in the same discharge or even other discharges with the same chopper setting. An example reference signal is shown in Figure 9(g).

The outline of the background and beam signal separation algorithm is the following. A modulation signal $S_{mod}(t)$ is generated for the whole processing time interval by repeating the reference signal as many times as the length of the measurement. The $S(t)$ measurement signal is modulated with the DC subtracted modulation signal therefore the frequency spectrum of the background is moved up to the chopping frequency and its harmonics and the beam signal is demodulated to low frequency. With an appropriate filter we extract the beam signal. The beam signal determined this way is multiplied with the modulation signal and subtracted from the original signal in order to obtain the background signal. In the first step a small part of the background signal leaks into the beam signal therefore the calculated background signal is subtracted from the original signal and the procedure is repeated.

The algorithm is implemented in practice the following way. We assume that the measured signal S consists of a background (B) and a modulated beam signal $L(t)$:

$$S(t) = B(t) + L(t)S_{mod}(t). \tag{6}$$

The reference signal is extended before the first sample with the end part of itself as shown in Figure 10 in a way that the beam-on time interval is in the middle of the extended reference signal $S_{ref,ext}$. A modulated measurement signal is generated:

$$S_M(t) = S(t) \cdot \left[S_{mod}(t) - \langle S_{ref,ext} \rangle\right]. \tag{7}$$

This signal is averaged for overlapping periods of $S_{ref,ext}$ to yield a signal $L_0(t)$ with T time resolution. Substituting Equation (6) into (7) and averaging for periods of $S_{ref,ext}$ one can see that for constant background the $L_0(t)$ signal has no contribution from the background. Assuming that the beam signal is also constant in one $S_{ref,ext}$ period the first approximation of the beam signal is

$$L(t) = \frac{L_0(t)}{\langle S^2_{ref,ext} \rangle - \langle S_{ref,ext} \rangle^2}. \tag{8}$$

The exact sampling time instance for this signal inside a chopper period is determined as

$$\Delta t = \frac{\int t' S^2_{ref,ext}(t') dt'}{\int S^2_{ref,ext}(t') dt'}, \tag{9}$$

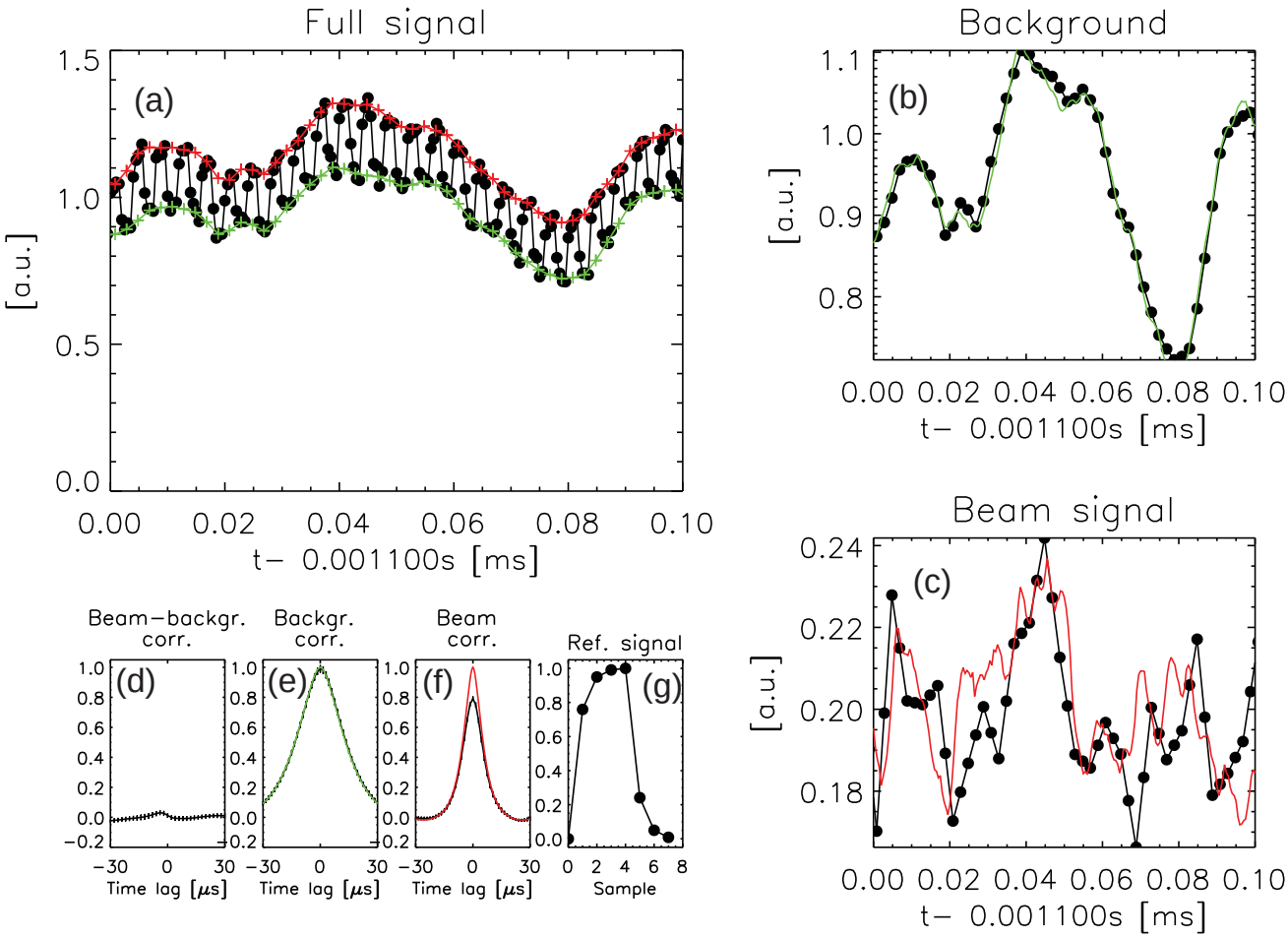

FIG. 9. Results of processing of simulated fast choppper measurement. Parameters of signal generation are SBR=0.2, badwidth of background signal: 20 kHz, bandwidth of beam signal: 50 kHz, SNR=60. (a) Signal (black with dots) with reconstructed background (green) and reconstructed background+beam signal (red). (b) Reconstructed (black with dots) and original (green) background signal. (c) Reconstructed (black with dots) and original (red) signal. (d) Correlation function of reconstructed beam and background signal. (e) and (f) Autocorrelation functions of reconstructed (black) and original (green, red) background and beam signals, respectively. (g) Reference signal $S_{ref}(t)$.

where t' is measured from the start of S_{ref} which we call the start of a chopper period. This L beam signal is linearly interpolated to the original signal timescale, multiplied by S_{mod} and subtracted from the measurement signal to yield a beam corrected background signal on the timescale of the original measurement. This is multiplied by $1 - S_{mod}$ and averaged

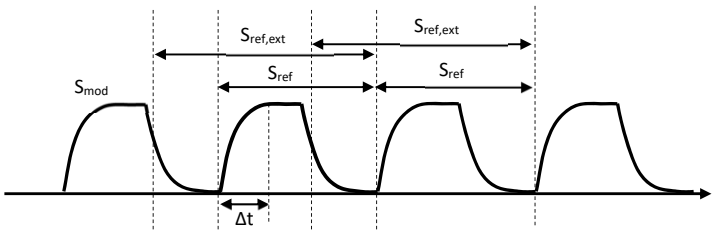

FIG. 10. Explantion for fast chopper processing. The S_{ref} periods follow each other while the $S_{ref,ext}$ periods are ovelapping. The beam-on time is in the middle of $S_{ref,ext}$.

for overlapping pieces equal the length of $S_{ref,ext}$ but starting one sample after the start of the chopper period. This averaging time interval is selected as it is symmetric around a beam-off time. The resulting signal is $B(t)$, the first approximation of the background with T time resolution. The exact sampling time instance for this signal inside a chopper period is determined similarly to Eq. (9) but using $1 - S^2_{ref,ext}$ for weighting. The first step of the algorithm creates a small spurious beam signal proportional to the time derivate of the background. This is corrected iteratively by subtracting the appropriately interpolated background signal from the original signal and repeating the above procedure once more. This yields a correct background and beam signal. Finally both signals are linearly interpolated to a common timescale with resolution equal to half the modulation period time. The timescale in this final interpolation is chosen the same for all the beam and background signals in the measurement therefore 128 beam and background signals are calculated on the same timescale. Although this processing algorithm is relatively complicated it is necessary as the maximum chopping frequency (250 kHz) is close to the bandwidth of the amplifiers. This way the signal does not change instanenously between the beam off and beam on states, it is not possible to just select a beam on and a beam off sample. Additionally due to the finite beam velocity the chopping period is slightly shifting in time between channels and therefore it is not possible to set the sampling times to to a fixed position in the chopping period. Increasing the amplifier bandwidth would introduce more noise in the measurement, while reducing the chopping frequency would increase crosstalk between the background and beam signal.

This processing method was tested on simulated signals. A background and a beam signal is generated as two independent random data series filtered with different lowpass filters.

A modulation signal is generated from a square wave lowpass filtered with the amplifier bandwidth. The beam signal is modulated, multiplied with SBR (Signal to Background Ratio) and added to the background signal. Finally a random band-limited noise is added to model the photon statistical and amplifier noise. The modeled signal is processed with the above described method and the original and extracted signals are plotted. Also correlation functions are calculated between the original and extracted signals and between the extracted beam and background signal. A somewhat extreme example is shown in Figure 9 where the background signal is 5 times the beam signal. The correlation functions show that the background signal is perfectly determined while the high-frequency part of the beam signal is lost to some extent. This is partly due to the higher frequency of the beam signal and partly to the noise which has 8% amplitude relative to the beam signal. Even in this case negligible correlation is seen between the calculated beam and background signal indicating that the fast modulation measurement does not mix these two. In other cases when the SBR is higher the beam signal is much better reconstructed.

VI. FIRST RESULTS

This section intends to illustrate the technical capabilities of the diagnostic through a few examples. Due to space limitations we do not intend to present here methods and considerations for plasma density calculation from the beam light profile.

The beam width and penetration was already shown in Figure 5. In spite of the approximately 4 m distance between the ion source and the observation volume the beam is about 2.5-3 cm wide, which is comparable to the poloidal measurement range of the APD system. The APD signal level corresponds well to expectations from modeling. At the peak of the light profile the beam signal is 0.2-0.3 V which means maximum $1 \cdot 10^{10} ph/s$ detected light flux in one pixel. In the edge-core region the signal noise is dominated by photon statistics and the SNR reaches 50-60. In the SOL the approximately 2.7 mV amplifier noise sets the noise but it still means around SNR=10 at the full 500 kHz bandwidth.

Additional noise can appear if Neutral Beam Injection (NBI) heating is applied on EAST. In this case neutrons are generated from beam-plasma interaction and they induce some pulses in the APD detectors as they are located close to the machine without neutron shielding. The pulse rate is maximum $10^3 s^{-1}$ and they can be removed by software post-

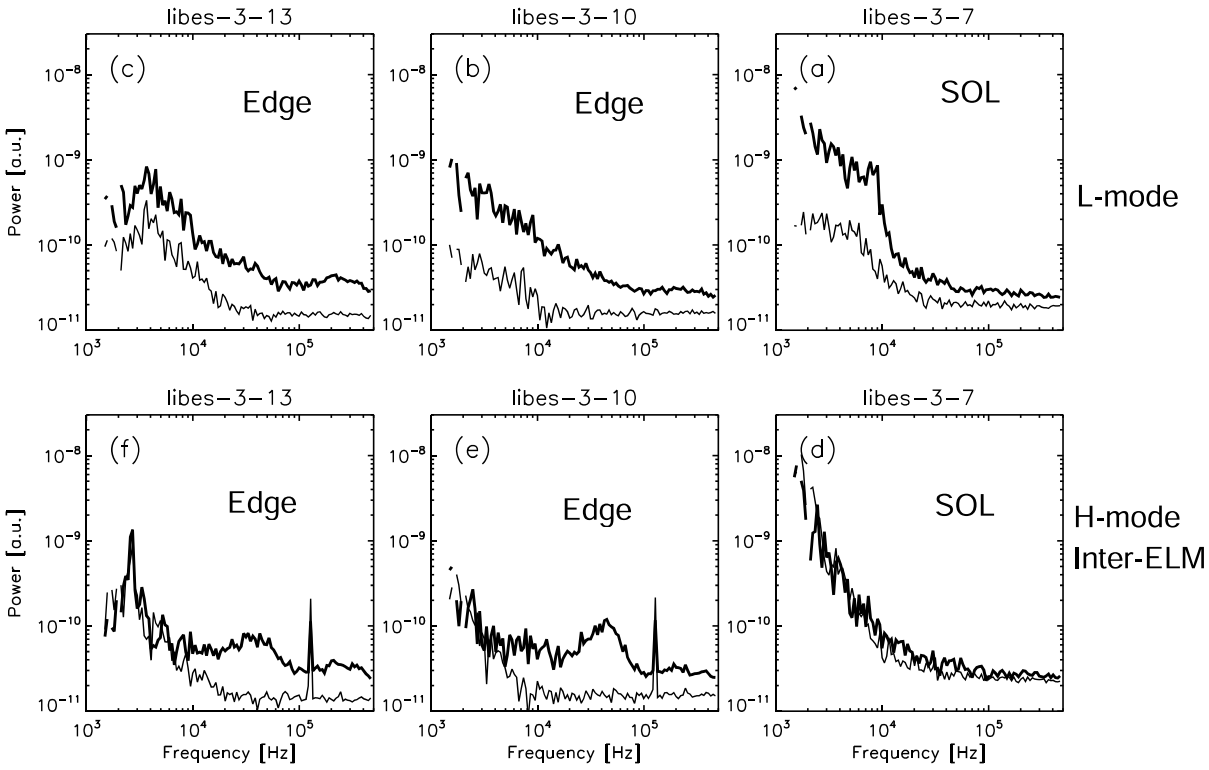

FIG. 11. Power spectra of three uncalibrated APD signals in APD row 3 in shot 66627 when the beam is on (thick line) and when it is off (thin line). The upper row is in L-mode (1.5-1.55s for beam-on and 1.45-1.5s for beam off), the lower row is between ELMs in H-mode (1.65-1.9 s). Channel 3-7 is in the close SOL, 3-10 is in the edge and 3-13 is an additional 3 cm inside. The power spectra have logarithmic frequency resolution, that is the size of frequency bins increase proportionally to the frequency.

processing as it is done in the KSTAR[28] and MAST[32] BES systems. It is expected that the radiation induced pulse rate will stay below $10^4 s^{-1}$ even with increased NBI heating power.

With slow beam chopping (few hundred Hz) statistical properties of plasma turbulence can be studied. Example power spectra are shown in Figure 11 for the same discharge and time interval shown in Figure 8. In the SOL (channel 3-7) power spectra extend to a few 10 kHz, background and beam signals have similar spectra. This is due to the fact that background is modulated by SOL filaments. In the edge plasma turbulence extends to higher frequencies. In H-mode between ELMs the background increases below 10 kHz and the SOL beam signal drops probably due to decreased transport into the SOL. In the edge plasma a broadband turbulence peak appears which is often present in H-mode A strong localized

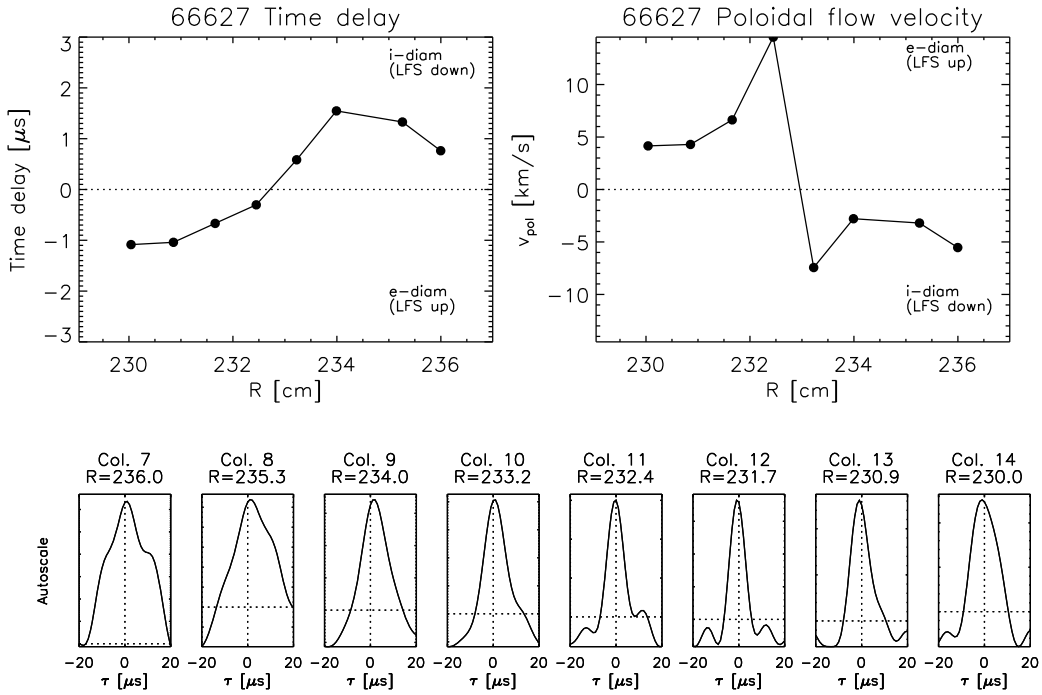

FIG. 12. Mean time delay $\overline{\tau_D}$ of turbulence in the 10-100 kHz frequency range between poloidally neighbouring channels and poloidal velocity profile $\overline{dZ}/\overline{\tau_D}$ as a function of the channel radial location. The crosscorrelation functions between poloidally neighbouring channels averaged for pixel columns are shown in the bottom. Data are from shot 66627, timerange 1.5-1.52s. APD columns 7-15 are processed.

peak at about 120 kHz with unknown origin is present in the background signal only in the divertor region. These spectra show that the EAST Li-BES diagnostic can measure plasma turbulence in the whole SOL-edge region.

The poloidal resolution of the diagnostic enables determination of the poloidal velocity of turbulence using time delay estimation (TDE). Figure 12 shows an example. To calculate the time delay all signals are filtered for the 10-100 kHz band by a FIR digital filter. The 3 cross-correlation functions between neighboring pairs of pixels in one column are calculated and averaged. The maximum location $\overline{\tau_D}$ of the mean correlation function is determined by fitting a second order polynomial to the 3 points around the maximum value. From this the poloidal flow velocity is calculated as $\overline{dZ}/\overline{\tau_D}$, where $\overline{dZ}$ is the mean vertical (poloidal) distance between the channel pairs in one column. The flow velocity shows a clear sign

reversal at about $R = 233cm$, at the separatrix position shown in Figure 4. This corresponds to the shear layer observed with Langmuir probes. The outermost point in the SOL has low signal and the background distorts the measurement. It has to be noted that the inclined effective observation volumes shown in Figure 6 could mix the poloidal and radial velocities in the TDE process if the correlation length of turbulence is smaller than the size of the sensitivity areas shown in Figure 6. In the present case the correlation lenght of beam light fluctuation is longer both in the radial and poroidal direction than the sensitivity contours, therefore little mixture of the radial and poloidal velocities is expected. On the other hand in the radial direction the finite timescale of beam atomic physics processes causes longer radial correlation length of the beam light fluctuations than the density fluctuations. The result is some smearing of the $\overline{\tau_D}(R)$ profile which causes higher poloidal velocities around the shear layer. For an exact calculation of the velocity profile around the shear layer the shape of the sensitivity areas and atomic physics processes have to be taken into account as well.

In the above examples time and frequency intervals were selected where the beam signal dominates over the background signal. If this is not the case fast beam chopping should be used and the beam and background signal separated as described in Section V. This technique is applicable if the frequency of phenomena is below half the chopping frequency or preferably even lower. This is the case in ELMs where the typical timescale of the signal evolution is a few hundred microsecond. A typical ELMy plasma measurement case as shown in Figure 8. A single ELM is analyzed in Figure 13. Here signals with relative amplitude calibration are processed. As the calibration takes into account all effects including the filter transmission it artificially increases the background intensity at the edge where the filter starts to cut the beam emission due to its small Doppler shift. A 600 μs long part of the signal is plotted during a single ELM, APD rows 2 and 3 are summed up. Only signals from 15 APD columns are shown as the signal change is the strongest there. The background corrected beam signals are shown on (a), plotted with constant offset above each other. The same plot is shown of the background signals on (c). The ELM happens in the middle of the time interval. The first sign of the perturbation is observable in the beam signals in the steep part of profile, where the signals are separated more due to the increasing mean level. To follow the changes a few radial light profiles are shown on plots (b) and (d). The good quality of the calibration is shown by the fact that the profiles are

smooth even with the short 10 μs integration time. These profiles show that the ELM starts with a few mm in-out movement of the profile at the time marked by the dotted line. Due to the steep gradient this causes a well observable oscillation in the pedestal signals. The material ejection into the SOL occurs at the last profile, when the SOL density increases. The drop in the beam signal at the peak is a mixture of density drop in the pedestal and increased beam attenuation due to higher SOL density. Towards the core plasma the drop in the signal is due to increased beam attenuation. It is interesting to see that the radial propagation of this ejection front is very fast in the order of 5 km/s. It is also worth noting that the background signal increases more gradually than the beam signals indicating that the background is not a function of local plasma parameters.

VII. CONCLUSIONS

This paper presented a Lithium Beam Emission Spectroscopy diagnostic for measuring the fast changes of the Scrape Off Layer (SOL) and edge plasma density in the EAST tokamak. The observation geometry is a compromise among large light collection solid angle, two-dimensional (radial-poloidal) resolution, acceptable spatial smearing and sufficient Doppler shift for suppression of background from unshifted Lithium line radiation. A 4×32 (poloidal$\times$radial) Avalanche Photodiode camera is used as main detector complemented by a CMOS camera for beam shape monitoring. A fast beam chopping technique allows removal of background light changes on few microsecond timescale even if the Signal to Background Ratio is considerably below 1. The results show that the collected light signal is sufficient to resolve the beam light changes with a few microsecond time resolution. Measurement of plasma turbulence and its poloidal flow velocity is demonstrated in both the SOL and edge region. Fast transients preceding ELMs and details of the plasma ejection during ELMs are resolved and will provide important information on these phenomena.

VIII. ACKNOWLEDGEMENTS

The excellent optical design of OMI OPTIKA Kft is highly acknowledged. This work has been carried out within the framework of the EUROfusion Consortium and has received funding from the Euratom research and training programme 2014-2018 under grant agree-

ment No 633053. The views and opinions expressed herein do not necessarily reflect those of the European Commission. Some technologies used in this diagnostic have been developed with support of the Hungarian National Development Agency under grant NUKENERG-OMFB-00717/718/719/2005.

REFERENCES

[1]G.S. Xu, V. Naulin, W. Fundamenski, C. Hidalgo, J.A. Alonso, C. Silva, B. Gonalves, A.H. Nielsen, J. Juul Rasmussen, S.I. Krasheninnikov, B.N. Wan, M. Stamp, and JET EFDA Contributors. Blob/hole formation and zonal-flow generation in the edge plasma of the jet tokamak. *Nuclear Fusion*, 49(9):092002, 2009.

[2]D. Carralero, P. Manz, L. Aho-Mantila, G. Birkenmeier, M. Brix, M. Groth, H. W. Müller, U. Stroth, N. Vianello, and E. Wolfrum. Experimental validation of a filament transport model in turbulent magnetized plasmas. *Phys. Rev. Lett.*, 115:215002, Nov 2015.

[3]S J Zweben, J A Boedo, O Grulke, C Hidalgo, B LaBombard, R J Maqueda, P Scarin, and J L Terry. Edge turbulence measurements in toroidal fusion devices. *Plasma Physics and Controlled Fusion*, 49(7):S1, 2007.

[4]I. Cziegler, J. L. Terry, J. W. Hughes, and B. LaBombard. Experimental studies of edge turbulence and confinement in alcator c-mod. *Physics of Plasmas*, 17(5):056120, 2010.

[5]G Fuchert, G Birkenmeier, D Carralero, T Lunt, P Manz, H W Mller, B Nold, M Ramisch, V Rohde, and U Stroth. Blob properties in l- and h-mode from gas-puff imaging in asdex upgrade. *Plasma Physics and Controlled Fusion*, 56(12):125001, 2014.

[6]I Cziegler, G R Tynan, P H Diamond, A E Hubbard, J W Hughes, J Irby, and J L Terry. Zonal flow production in the l-h transition in alcator c-mod. *Plasma Physics and Controlled Fusion*, 56(7):075013, 2014.

[7]I. Shesterikov, Y. Xu, G. R. Tynan, P. H. Diamond, S. Jachmich, P. Dumortier, M. Vergote, M. Van Schoor, G. Van Oost, and TEXTOR Team. Experimental evidence for the intimate interaction among sheared flows, eddy structures, reynolds stress, and zonal flows across a transition to improved confinement. *Phys. Rev. Lett.*, 111:055006, Aug 2013.

[8]N. C. Luhmann Jr., H. Bindslev, H. Park, J. Sanchez, G. Taylor, and C. X. Yu. Microwave diagnostics. *Fusion Science and technology*, 53(2):335, 2008.

[9]L. Schmitz, L. Zeng, T. L. Rhodes, J. C. Hillesheim, E. J. Doyle, R. J. Groebner, W. A. Peebles, K. H. Burrell, and G. Wang. Role of zonal flow predator-prey oscillations in triggering the transition to h-mode confinement. *Phys. Rev. Lett.*, 108:155002, Apr 2012.

[10]G. D. Conway, C. Angioni, F. Ryter, P. Sauter, and J. Vicente. Mean and oscillating plasma flows and turbulence interactions across the $l-h$ confinement transition. *Phys. Rev. Lett.*, 106:065001, Feb 2011.

[11]D. M. Thomas, G. R. McKee, K. H. Burrell, F. Levinton, E. L. Foley, and R. K. Fisher. Active spectroscopy. *Fusion Science and technology*, 53(2):487, 2008.

[12]G. R. McKee, R. J. Fonck, M. Jakubowski, K. H. Burrell, K. Hallatschek, R. A. Moyer, D. L. Rudakov, W. Nevins, G. D. Porter, P. Schoch, and X. Xu. Experimental characterization of coherent, radially-sheared zonal flows in the diii-d tokamak. *Physics of Plasmas*, 10(5):1712–1719, 2003.

[13]G R McKee, D K Gupta, R J Fonck, D J Schlossberg, M W Shafer, and P Gohil. Structure and scaling properties of the geodesic acoustic mode. *Plasma Physics and Controlled Fusion*, 48(4):S123, 2006.

[14]Y.-c. Ghim, A. A. Schekochihin, A. R. Field, I. G. Abel, M. Barnes, G. Colyer, S. C. Cowley, F. I. Parra, D. Dunai, and S. Zoletnik. Experimental signatures of critically balanced turbulence in mast. *Phys. Rev. Lett.*, 110:145002, Apr 2013.

[15]J Schweinzer, E Wolfrum, F Aumayr, M Pockl, H Winter, R P Schorn, E Hintz, and A Unterreiter. Reconstruction of plasma edge density profiles from li i (2s-2p) emission profiles. *Plasma Physics and Controlled Fusion*, 34(7):1173, 1992.

[16]R Fischer, E Wolfrum, J Schweinzer, and the ASDEX Upgrade Team. Probabilistic lithium beam data analysis. *Plasma Physics and Controlled Fusion*, 50(8):085009, 2008.

[17]E. Wolfrum, F. Aumayr, D. Wutte, HP. Winter, E. Hintz, D. Rusbüldt, and R. P. Schorn. Fast lithium-beam spectroscopy of tokamak edge plasmas. *Review of Scientific Instruments*, 64(8):2285–2292, 1993.

[18]Kent McCormick, Stefan Fiedler, Gábor Kocsis, Joseph Schweinzer, and Sándor Zoletnik. Edge density measurments with a fast li-beam probe on tokamak and stellarator experiments. *Fusion Engineering and Design*, 34-35:125, 1997.

[19]M Willensdorfer, G Birkenmeier, R Fischer, F M Laggner, E Wolfrum, G Veres, F Aumayr, D Carralero, L Guimaris, B Kurzan, and the ASDEX Upgrade Team. Characterization of the li-bes at asdex upgrade. *Plasma Physics and Controlled Fusion*, 56(2):025008, 2014.

[20]D. M. Thomas. Development of lithium beam emission spectroscopy as an edge fluctuation diagnostic for diii-d (invited). *Review of Scientific Instruments*, 66(1):806–811, 1995.

[21]S Zoletnik, S Fiedler, G Kocsis, G K McCormick, J Schweinzer, and H P Winter. Determination of electron density fluctuation correlation functions via beam emission spectroscopy. *Plasma Physics and Controlled Fusion*, 40(7):1399, 1998.

[22]S. Zoletnik, M. Anton, M. Endler, S. Fiedler, M. Hirsch, K. McCormick, and J. Schweinzer. Density fluctuation phenomena in the scrape-off layer and edge plasma of the wendelstein 7-as stellarator. *Physics of Plasmas*, 6(11):4239–4247, 1999.

[23]G Birkenmeier, F M Laggner, M Willensdorfer, T Kobayashi, P Manz, E Wolfrum, D Carralero, R Fischer, B Sieglin, G Fuchert, U Stroth, and the ASDEX upgrade team. Magnetic field dependence of the blob dynamics in the edge of asdex upgrade l-mode plasmas. *Plasma Physics and Controlled Fusion*, 56(7):075019, 2014.

[24]Sándor Zoletnik, Gábor Petravich, Attila Bencze, Miklós Berta, Stefan Fiedler, Kent McCormick, and Joseph Schweinzer. Two-dimensional density and density fluctuation diagnostic for the edge plasma in fusion devices. *Review of Scientific Instruments*, 76:073504, 2005.

[25]S Zoletnik, L Bardoczi, A Krämer-Flecken, Y Xu, I Shesterikov, S Soldatov, G Anda, D Dunai, G Petravich, and the TEXTOR Team. Methods for the detection of zonal flows using one-point and two-point turbulence measurements. *Plasma Physics and Controlled Fusion*, 54(6):065007, 2012.

[26]M. Brix, D. Dodt, A. Korotkov, P. Morgan, D. Dunai, R. Fischer, A. Meigs, I. S. Nedzelskiy, J. Schweinzer, J. Vince, and S. Zoletnik. Upgrade of the lithium beam diagnostic at jet. *Review of Scientific Instruments*, 81(10):10D733, 2010.

[27]S Zoletnik, Cs. Buday, D. Dunai, S. Kálvin, A. Krämer-Flecken, Y. Liang, G. Petravich, S. Soldatov, J. Pearson, D. Rfy, and TEXTOR Team. Dynamics of the electron density profile and plasma turbulence during the l-h transition and elms in textor. *Eurofphysics Conference Abstracts*, 36F:O3.107, 2012.

[28]M. Lampert, G. Anda, A. Czopf, G. Erdei, D. Guszejnov, . Kovcsik, G. I. Pokol, D. Rfy, Y. U. Nam, and S. Zoletnik. Combined hydrogen and lithium beam emission spectroscopy observation system for korea superconducting tokamak advanced research. *Review of Scientific Instruments*, 86(7):073501, 2015.

[29]G Anda, D Dunai, M Lampert, T Krizsanczi, J Nmeth, S. Bató, Y U Nam, G H Hu, and S Zoletnik. Development of a high current 60 kev neutral lithium beam injector for beam emission spectroscopy measurements on fusion experiments. *Review of Scientific Instruments*, page Submitted to Rev. Sci. Instrum.

[30]D. Guszejnov, G. I. Pokol, I. Pusztai, D. Refy, S. Zoletnik, M. Lampert, and Y. U. Nam. Three-dimensional modeling of beam emission spectroscopy measurements in fusion plasmas. *Review of Scientific Instruments*, 83(11):113501, 2012.

[31]M. Willensdorfer, E. Wolfrum, R. Fischer, J. Schweinzer, M. Sertoli, B. Sieglin, G. Veres, and F. Aumayr. Improved chopping of a lithium beam for plasma edge diagnostic at asdex upgrade. *Review of Scientific Instruments*, 83(2):023501, 2012.

[32]A. R. Field, D. Dunai, R. Gaffka, Y. c. Ghim, I. Kiss, B. Mszros, T. Krizsanczi, S. Shibaev, and S. Zoletnik. Beam emission spectroscopy turbulence imaging system for the mast spherical tokamak. *Review of Scientific Instruments*, 83(1):013508, 2012.

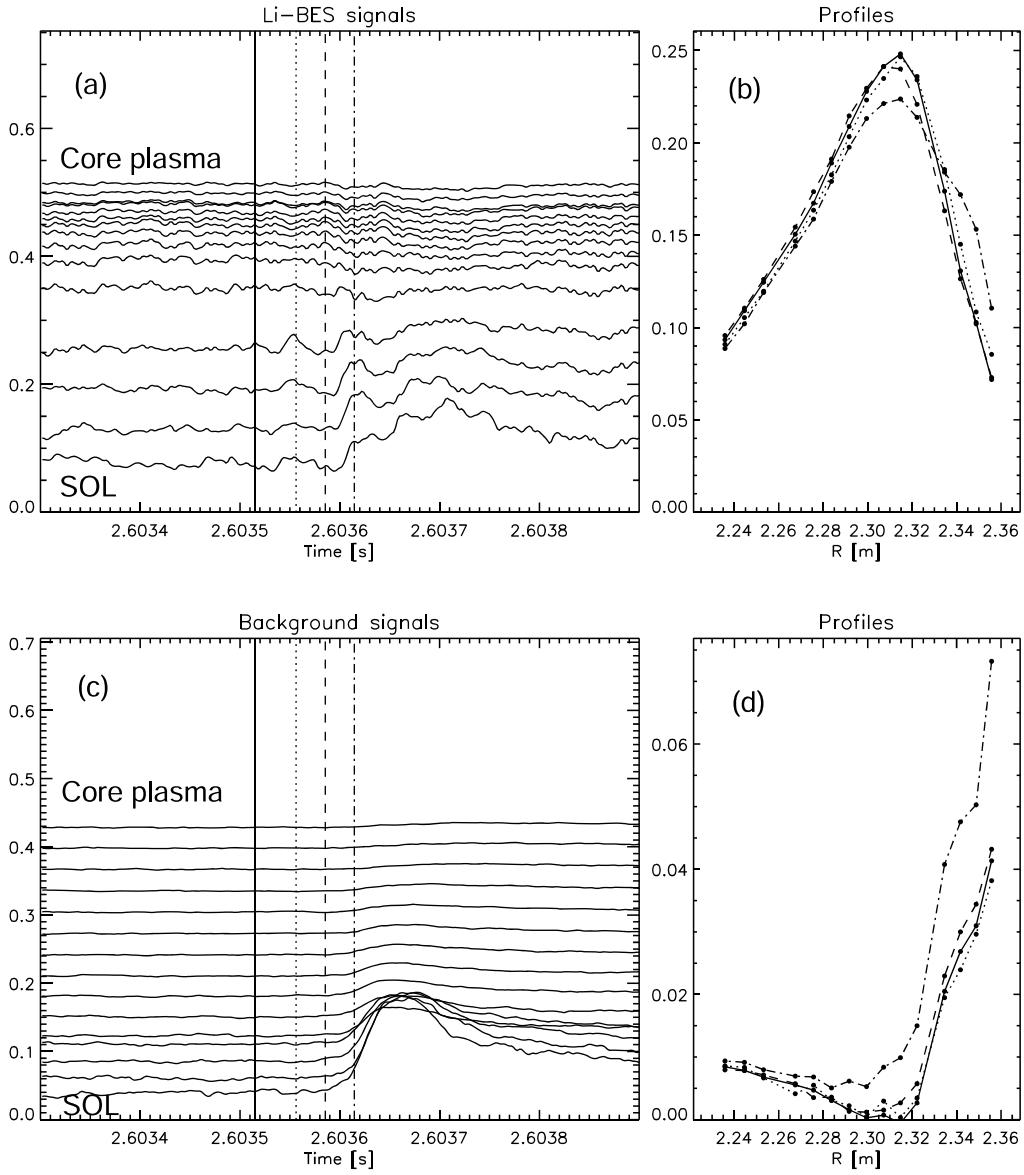

FIG. 13. Example of ELM measurement with fast chopping in shot 70677. (a) and (c) show the background corrected beam signals and background signals, respectively. The curves are shifted vertically by 0.03 between channels. Plots (b) andd(d) delineate the radial light distribution at selected times for the beam and background signals, repectively. Pixel columns 5-19 are processed and the plotted signals are the sum of signals in pixel rows 2,3. The profiles are taken at the times indicated by the same linestyle in the signal plot. All signals are integrated for 10 μs